



Effects of Magnetic Field Loops on the Dynamics of Advective Accretion Flows and Jets around a Schwarzschild Black Hole

Sudip K. Garain^{1,2} , Dinshaw S. Balsara¹, Sandip K. Chakrabarti³ , and Jinho Kim²

¹Department of Physics, University of Notre Dame, Notre Dame, IN 46556, USA; sgarain@nd.edu, sgarain@kasi.re.kr

²Korea Astronomy & Space Science Institute, 776 Daedeokdae-ro, Yuseong-gu, Daejeon 34055, Republic of Korea

³Indian Center for Space Physics, 43 Chalanika, Garia St. Rd., Kolkata, 700084, India

Received 2019 July 15; revised 2019 November 25; accepted 2019 November 26; published 2020 January 8

Abstract

Magnetic fields advected along with low angular momentum accretion flows predominantly become toroidal owing to the strong azimuthal velocity close to a black hole. We study self-consistently the movements of these flux tubes inside an advective disk and how they dynamically influence the flow. We find that the centrifugal barrier slows down the radial motion of the flux tubes. In this case, the large magnetic flux tubes with a significant drag force escape along the vertical axis owing to buoyancy. Magnetic pressure rises close to the black hole and, together with the centrifugal force, combats gravity. The tug-of-war among these forces causes the centrifugal-pressure-supported shock to oscillate radially. We study the effects of successive injection of flux tubes and find how the flux tube could be trapped inside the disk in regions of highest entropy. Most interestingly, the shock wave remains at its average location and is not destroyed. We show that the toroidal field loops contribute significantly to collimate and accelerate the outflows from the centrifugal barrier and suggest that this mechanism is a way to collimate and accelerate jets.

Unified Astronomy Thesaurus concepts: [Accretion \(14\)](#); [Nonrotating black holes \(1121\)](#); [Magnetohydrodynamical simulations \(1966\)](#); [Shocks \(2086\)](#)

Supporting material: animation

1. Introduction

Magnetic field is ubiquitous in nature. In the context of accretion flows in a binary system containing a black hole, it is likely that the companion star may have winds with entangled magnetic fields that are accreted by the black hole. As the accretion flow approaches the black hole, the azimuthal velocity of the flow increases, and in an ideal magnetohydrodynamic (MHD) limit, the spiraling flow stretches the field line and makes predominantly toroidal loops. As these loops come very close to the black hole, the radial velocity rises and becomes supersonic, stretching the field lines in a radial direction. Due to the drag effect, the radial motion of larger flux tubes is slowed down, and due to the buoyancy effect, they may leave the disk altogether (Chakrabarti & D’Silva 1994, hereafter [CD94](#); D’Silva & Chakrabarti 1994, hereafter [DC94](#)).

In the present paper, our goal is to carry out a self-consistent study of the dynamic behavior of these magnetic flux tubes inside an advective, low angular momentum flow around a Schwarzschild black hole. We also study the effects of these flux tubes on the flow. In the literature, qualitative studies of the role of the flux tubes in transporting angular momentum and creating a possible corona in an accretion flow have been done by Eardley & Lightman (1975), Galeev et al. (1979), Coroniti (1981), and Shibata et al. (1990). The dynamics of flux tubes in a steady disk has been studied in detail in [CD94](#) and [DC94](#), where the flux tubes have been assumed not to influence the dynamics of the flow. Forces such as the magnetic buoyancy and tension are included in those calculations. They demonstrated that if the flux tubes are very thin, then they can reach very close to the black hole; otherwise, they would leave the low angular momentum thick disk along the funnel wall.

It has long been speculated that the funnels in thick accretion disks (Lynden-Bell 1978; Paczyński & Wiita 1980) may be a

site to collimate the outflows and jets observed in active galactic nuclei and microquasars. Eggum et al. (1985) discussed radiative acceleration of jets from the funnel and found a maximum velocity of about $0.3c$, where c is the velocity of light. Fukue (1982) and Chakrabarti (1986) discussed acceleration of the jets using thermal and hydrodynamical processes. In all these cases the matter is supplied by the thick accretion disk, while collimation is done by the centrifugally driven vortices or funnel walls along the axis. Lovelace (1976), Blandford & Payne (1982), Chakrabarti & Bhaskaran (1992), Camenzind (1989), Heyvaerts & Norman (1989), Koide et al. (1999), and others show that magnetic fields may also contribute to the collimation of the outflows. Konigl (1989) showed that in some regions of the parameter space it is possible to obtain self-similar Blandford & Payne (1982) type jets that achieve super-Alfvénic velocity soon after the matter leaves the disk. In the recent simulations by general relativistic MHD codes, matter is usually launched from the disks threading poloidal magnetic fields and jets are produced (Nishikawa et al. 2005; McKinney 2006; Shafee et al. 2008; Tchekhovskoy et al. 2011). The nature of the source of such aligned large-scale magnetic field has not been discussed in these works, and results are found to be sensitive to the initial field configuration.

Since it is difficult to imagine, how, in the absence of poloidal fields of central black holes, a disk can have large-scale unidirectional poloidal fields, we are motivated to take up a realistic problem where such large-scale fields are not required in order to produce well-collimated and accelerated jets, provided that matter is injected from an advective disk. A low angular momentum advective flow moves rapidly and thus feels the centrifugal barrier very close to the black hole. The outer boundary of matter piled up at this barrier is the shock

front, and the post-shock region downstream behaves as a thick disk as shown more than two decades ago (Molteni et al. 1994) using a hydrodynamic simulation code. This thick disk is believed to produce the observed hard radiation from the accretion disk (Chakrabarti 1997 and references therein), and the oscillation of the centrifugal-pressure-supported shock boundary may cause the quasi-periodic oscillations (Molteni et al. 1996b; Chakrabarti et al. 2004; Garain et al. 2014) observed in light curves of several black hole binaries as revealed by the power-density spectra. Thus, efforts are ongoing to include magnetic field in this advective flow, which naturally produces thick disks as used in earlier days. After the work of CD94 and DC94, where the disk variables were predetermined, a recent work by Deb et al. (2017) studied the motion of flux tubes in a *hydrodynamic* time-dependent flow showing that the injection of a single flux tube increased the collimation of the jet as long as it did not escape. However, there was no attempt to study MHD flows or the effects of the fields on the dynamics of the accretion flow. In the present paper, we remove these deficiencies and answer the followings questions: (a) Can the toroidal field lines escape owing to buoyancy? (b) Are they capable of collimating and accelerating jets? (c) Are the standing shocks in an advective flow stable under these axisymmetric flux tubes? (d) Can there be a steady corona in an advective disk that may inverse Comptonize the flow? (e) Is there a way to anchor fields inside an advective disk? (f) Are there both steady jets and episodically ejected blobby jets in a magnetized flow? Of course, every numerical simulation also produces new results that are not anticipated before, and the present one is no exception. We will discuss them and their implications in the final section.

In the next section, we shall present numerical method used in our simulations. In Section 3, we present the results, and in Section 4, we present the concluding remarks.

In this paper, we choose $r_g = 2GM_{\text{bh}}/c^2$ as the unit of distance, $r_g c$ as the unit of angular momentum, and r_g/c as the unit of time. Here G is the gravitational constant and M_{bh} is the mass of the black hole. In addition to these, we choose the geometric units $2G = M_{\text{bh}} = c = 1$. Thus $r_g=1$, and angular momentum and time are measured in dimensionless units.

2. Numerical Methods

In order to study the magnetized sub-Keplerian advective disk, we solve the nonrelativistic ideal MHD equations in cylindrical coordinates. A realistic disk is three-dimensional. However, assuming axisymmetry, we simplify the problem and solve these equations numerically in the R - Z plane. The full set of equations can be written in the conservation form as follows (Ryu et al. 1995b; Balsara 2004):

$$\frac{\partial \rho}{\partial t} + \nabla \cdot (\rho \mathbf{v}) = 0 \quad (1)$$

$$\frac{\partial (\rho \mathbf{v})}{\partial t} + \nabla \cdot \left(\rho \mathbf{v} \otimes \mathbf{v} + \left(P + \frac{\mathbf{B}^2}{8\pi} \right) \mathbf{I} - \frac{\mathbf{B} \otimes \mathbf{B}}{4\pi} \right) = -\rho \mathbf{g} \quad (2)$$

$$\frac{\partial E}{\partial t} + \nabla \cdot \left(\left(E + P + \frac{\mathbf{B}^2}{8\pi} \right) \mathbf{v} - \frac{(\mathbf{B} \cdot \mathbf{v}) \mathbf{B}}{4\pi} \right) = -\rho \mathbf{v} \cdot \mathbf{g} \quad (3)$$

$$\frac{\partial \mathbf{B}}{\partial t} - \nabla \times (\mathbf{v} \times \mathbf{B}) = 0. \quad (4)$$

Here, ρ is density, P is the thermal pressure, \mathbf{v} is the velocity, \mathbf{B} is the magnetic field, \mathbf{I} is the identity tensor, \mathbf{g} is the gravitational acceleration, and

$$E = \frac{1}{2} \rho v^2 + \frac{P}{\gamma - 1} + \frac{\mathbf{B}^2}{8\pi}$$

is the energy.

We use the second-order-accurate RIEMANN code (Balsara 1998a, 1998b, 2004, 2009; Balsara & Spicer 1999b, 1999a; Balsara et al. 2009, 2013) to solve the ideal MHD equations. Spatial reconstruction has been carried out using the MC limiter, and the HLL Riemann solver has been used for flux calculations. In addition, the multidimensional Riemann solver has been used for edge-averaged electric field evaluations. The matching time accuracy has been achieved following the predictor-corrector step. To model the initial injection, we assume an accretion flow of a gas around a nonrotating black hole located at the center of the cylindrical coordinate system. The gravitational potential of the central black hole is modeled using the pseudo-Newtonian potential given by Paczyński & Wiita (1980),

$$\psi(r) = -\frac{1}{2(r-1)},$$

where $r = \sqrt{R^2 + Z^2}$. We also assume a polytropic equation of state for the accreting gas, $P = K\rho^\gamma$, where $\gamma = 4/3$ is the adiabatic constant. K is the measure of entropy and is allowed to change inside the disk.

Since we are interested in the region very close to the central black hole, the simulations are performed on a $[2: 100]r_g \times [-50: 50]r_g$ computational domain in the R - Z plane using a uniformly spaced 1024×1024 zone mesh. Incoming matter enters the computational domain through the right radial boundary at $R_{\text{out}} = 100r_g$. The incoming matter injected at the right boundary points toward the central black hole. The radial speed $v_{\text{in}} = \sqrt{v_R^2 + v_Z^2}$ of the incoming matter is the same at all heights. We also use the same sound speed a_s at all heights (Molteni et al. 1996a). The values of v_{in} and a_s are calculated following Chakrabarti (1989, 1990) assuming the vertical equilibrium model, as they depend on the specific energy ϵ and specific angular momentum λ of the incoming matter. The interior of the computational domain is initialized with a low density given by $\rho_{\text{floor}} = 10^{-6}$. The initial low pressure $P_{\text{floor}} = a_s^2 \rho_{\text{floor}}^\gamma$ is chosen such that the sound speed inside the computational domain is the same as the sound speed a_s at the outer boundary. The initial density and pressure in the computational domain are to some extent irrelevant because the injected sub-Keplerian flow will wash out this initial condition in several dynamical times. On the left radial boundary at $R_{\text{in}} = 2r_g$, we use the outflow boundary condition so as to suck matter inside the black hole (Hawley 2000; Hawley & Krolik 2001). It may be possible that such a boundary condition will affect the amount of poloidal magnetic flux accumulation near the axis, especially when the magnetic field strength is high. However, for most cases, we find that along the $R_{\text{in}} = 2r_g$ axis the poloidal velocity is greater than the Alfvén speed. Therefore, we believe that, except for strong magnetic field, the influence of the inner boundary on the flow

Time=17578

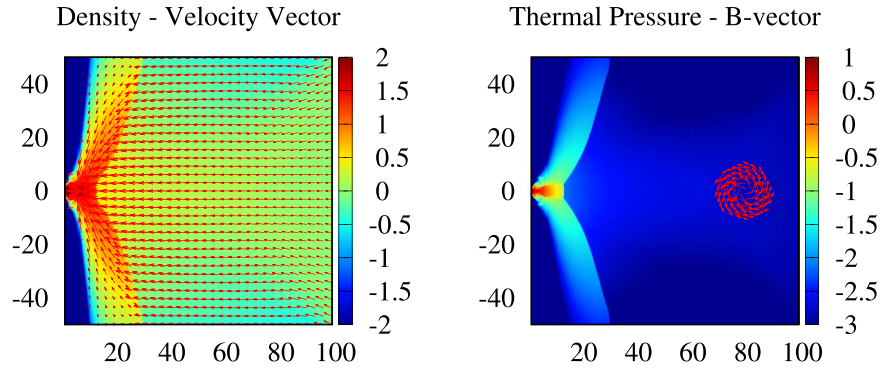


Figure 1. Left panel: density distribution, in log scale, overlaid with velocity field vectors. Right panel: thermal pressure distribution, in log scale, overlaid with magnetic field vectors. The animation shows the propagation of four successive flux ropes through the sub-Keplerian accretion disk and their effects on the flow dynamics. The animation runs from time 16,378 to 69,962. The duration of the animation is 27 s.

(An animation of this figure is available.)

is limited. Also, we use only the outflow boundary condition on the top and bottom Z-boundaries, as the injected matter behaves as a hot puffed-up disk close to a black hole. No matter is allowed to enter through the top and bottom Z-boundaries.

It is pertinent to ask whether the outflow is affected by the top and bottom Z-boundaries. Indeed, this would be true for any simulation with outflow. However, for this particular sub-Keplerian model, a very detailed analysis on the boundary conditions has been carried out in Section 4 of Ryu et al. (1995a). Subsequently, similar boundary conditions have been used in many other works, e.g., Molteni et al. (1996a), Ryu et al. (1997), Giri et al. (2010), Garain et al. (2012), Giri & Chakrabarti (2013), Lee et al. (2016), etc. In these works, the Z-boundaries are placed at various heights ranging from $50r_g$ to $200r_g$. We have used the same Z-boundary boundary conditions as in these works. Therefore, we believe that the boundary conditions are not affecting the formation and sustenance of the outflow. Detailed visual inspection of the simulated images also support the same conclusion. Readers are directed to see the movie in Figure 1 for run A2, which is available online. (Additionally, it is also available at <https://youtu.be/upWm9dFrkt4>.)

We use a hydro-steady state as the initial condition for our magnetized accretion flow simulations. The hydro-steady state is achieved by running the code for ~ 10 dynamical times without magnetic field. The dynamical time is defined as the time taken by the matter entering at the outer radial boundary of our computational domain to reach the black hole horizon when the flow has achieved a steady state. In Section 3, we will show the hydro-steady states that develop with an accretion shock.

Magnetic fields are very pervasive in astrophysical plasma, and it is inevitable that the magnetic fields will be dredged in with the accretion flow. We will thus study the effects of episodic magnetic flux rope injection on this hydro-steady state that develops as a consequence of sub-Keplerian inflow. Specifically, we are interested in checking whether the outflow rate is enhanced as a result of enhanced magnetic fields in the inflow. In this paper, we study the effects of episodic inflow of magnetic flux tubes. This hopefully mimics the realistic situation when magnetic fields of various cross sections and strengths are randomly injected continuously into the accreting gas. Similar work has been reported in Kudoh et al. (2002), where they studied jet formation from an accretion disk with

Table 1
Parameters Used for the Simulations

Case	λ	β	v_{in}	a_s	$v_\phi = \frac{\lambda}{R_{out}}$
A1	1.65	50	0.04862	0.04446	0.0165
A2	1.65	25	0.04862	0.04446	0.0165
A3	1.65	10	0.04862	0.04446	0.0165
B1	1.5	50	0.04916	0.04445	0.015
B2	1.5	25	0.04916	0.04445	0.015
B3	1.5	10	0.04916	0.04445	0.015

initial poloidal magnetic field loops. However, our simulation setup is significantly different compared to this work. In our work, the disk has significant radial velocity, and our flux tubes have an initial toroidal component in addition to poloidal component.

The magnetic flux ropes, with a helical field, are episodically set up inside the computational domain. We use the following magnetic vector potential to set up the in-plane components B_R and B_z of the initial magnetic flux ropes.

$$A_\phi = \begin{cases} -\sqrt{(4\pi)(10 - r_{ab})} & \text{for } r_{ab} \leq 10, \\ 0 & \text{for } r_{ab} > 10, \end{cases} \quad (5)$$

where $r_{ab} = \sqrt{(R - a)^2 + (Z - b)^2}$, a and b being the coordinates of the center of the flux ropes. In addition to these, a toroidal component $B_\phi \sim \frac{1}{R}$ is added. These field components are rescaled later so that the average plasma beta matches with the desired value inside the region surrounded by the flux ropes. We set up multiple episodes of magnetic field injection, and some of our longer-running simulations have four episodes where magnetic field is injected. To break the symmetry, the flux ropes are randomly injected above or below the midplane of the simulation.

3. Results

In Table 1, we document the parameters that are used for the simulations presented here. The specific energy $\epsilon = 0.0021$ is assumed for all the cases. We consider two different specific angular momenta $\lambda = 1.65$ and $\lambda = 1.5$, which are much lower as compared to the marginally stable value of 1.83. So,

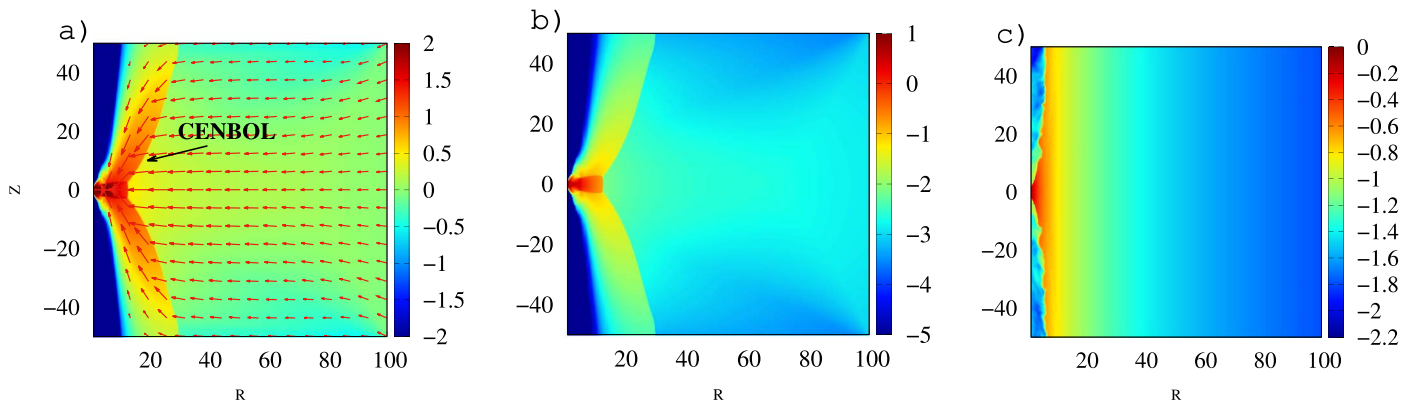


Figure 2. Initial hydro-steady state for the simulation runs A1, A2, and A3. (a) Density distribution in logarithmic scale overlaid with momentum vectors. The length of the vectors is proportional to the magnitude of the momentum. The centrifugal-pressure-supported boundary layer (CENBOL) can be seen close to the black hole, where there is a sudden jump in color in density. (b) Pressure distribution in log scale. The CENBOL is found to bend outward as one moves away in the vertical direction. (c) Distribution of the toroidal velocity in log scale inside the disk. For our nonviscous simulations, the specific angular momentum remains conserved. As the matter approaches the black hole, its rotational velocity increases.

under the normal circumstances, even a zero energy and zero viscosity flow will allow the matter to fall onto the black hole without any obstruction. For $\lambda = 1.65$, we have $v_{\text{in}} = 0.048$ and $a_s = 0.044$ as the injection parameters for cases A1, A2, and A3. For $\lambda = 1.5$, we have $v_{\text{in}} = 0.049$ and $a_s = 0.044$ for cases B1, B2, and B3. Nonmagnetized flow with $\lambda = 1.5$ does not show the formation of shock in a flow in vertical equilibrium. However, we see that a gas becomes dense owing to the centrifugal barrier. On the other hand, for $\lambda = 1.65$, we see the formation of a steady shock at $13r_g$ on the equatorial plane. The post-shock region is subsonic and hot and is the location where the thermal energy of the inflow is efficiently dissipated in the presence of soft (low-energy) seed photons. This is also the region that supplies matter to outflows. This region is known as the CENtrifugal pressure dominated BOUNDary Layer (CENBOL). For each angular momentum mentioned above, we run three MHD simulations with the magnetic field loops having average plasma betas given by $\beta = 50, 25$, and 10 . Here plasma beta is defined as $\beta = P_{\text{gas}}/P_{\text{mag}}$, where P_{gas} is the gas pressure and P_{mag} is the magnetic field pressure. Therefore, these cases give us an opportunity to study the effects of increased magnetic field strength on the accretion disk.

Figure 2(a)–(c) shows the initial hydro-steady state for the simulation runs A1, A2, and A3. Figure 2(a) shows the density distribution, in log scale overlaid with momentum vectors. The length of the vectors is proportional to the magnitude of the momentum. The CENBOL can be identified by the jump in color of density. The CENBOL is bent outward as one moves away in the vertical direction from the equatorial region because the gravitational pull is decreased with increasing distance from the black hole. Figure 2(b) shows the pressure distribution, again in log scale, inside the accretion disk. Here, again, we can identify the shock front (i.e., CENBOL boundary). Figure 2(c) shows the distribution of the toroidal velocity in log scale inside the disk. In our nonviscous simulations, the specific angular momentum remains conserved, and as a result, as the matter approaches the black hole, its rotational velocity increases.

Figure 3 shows the initial hydro-steady state for the simulation runs B1, B2, and B3. As in Figure 2(a), here also we can identify the CENBOL in Figure 3(a). Note that the

parameters used for this simulation do not allow shock formation theoretically when the vertical equilibrium model is used. However, we find that matter indeed slows down because of the centrifugal force forming the CENBOL. Figure 3(b) shows the pressure distribution in the log scale inside the accretion disk, and Figure 3(c) shows the distribution of the toroidal velocity, again in a log scale, inside the disk.

3.1. Propagation of Flux Ropes through Sub-Keplerian Flow

For cases A1, A2, B1, and B2, we have four episodes of flux rope injection at four successive times. For case A1, the flux ropes are injected at times 17,578, 26,930, 36,529, and 46,388. For case A2, the flux ropes are injected at times 17,578, 32,965, 45,605, and 57,961. For case B1, the flux ropes are injected at times 22,227, 33,312, 46,372, and 59,242. For case B2, the flux ropes are injected at times 22,227, 37,581, 53,079, and 67,045. For all these cases, the centers of the flux ropes are placed at four different locations given by the $[R, Z]$ coordinates as $[80, 0]$, $[85, 20]$, $[85, -22]$, $[80, 0]$ inside the accretion disk. For case A3, we have one injection at time 17,578 and the center is placed on the equatorial plane at $[80, 0]$. For case B3, we have two injections at two successive times at 22,227 and 33,254, and the centers are placed at $[80, 0]$ and $[85, 20]$, respectively. Because of the stronger magnetic fields in cases A3 and B3, they run with incredibly small time steps, especially when the magnetic field reaches the CENBOL region. For this reason, we were not able to explore many episodes of field injection in those two runs. The radius of the outer rope is $10r_g$ at injection in all the cases. The flux ropes are initialized so that they are in pressure equilibrium with the surrounding material. Thus, the matter density in the region surrounded by the magnetic field lines is reduced in such a way that the sum of the thermal and magnetic pressure is the same as the thermal pressure before initialization of magnetic flux ropes. This ensures pressure balance with surrounding material inside the sub-Keplerian disk. The accretion flow carries the flux ropes toward the central object. Since the accretion flow is mainly in the radial direction, our experience has been that it does not matter too much whether the magnetic flux ropes are injected above or below the midplane.

As the flux ropes radially propagate through the sub-Keplerian disk, we notice that the flux ropes are stretched in the

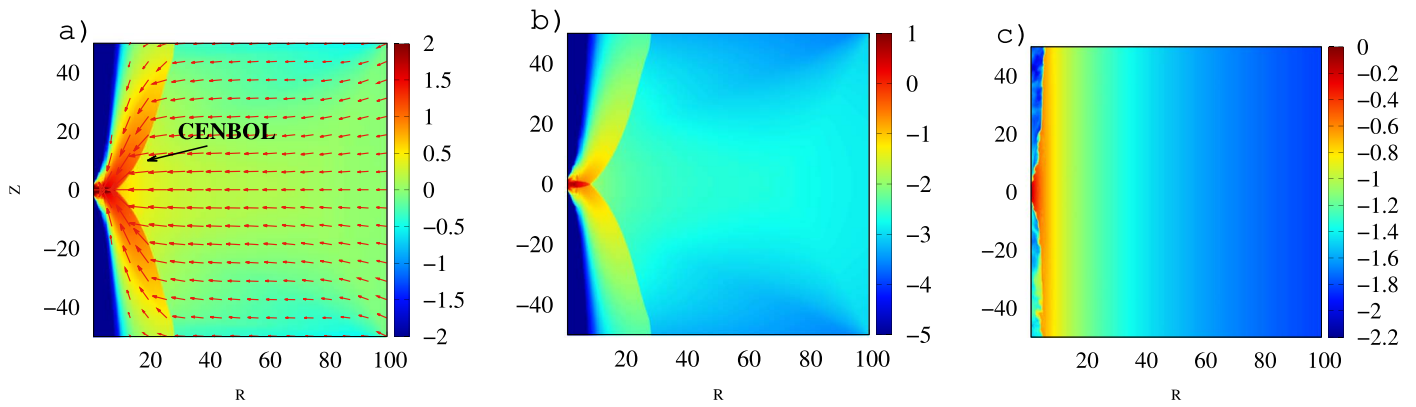


Figure 3. Same as Figure 2, however, for the simulation runs B1, B2, and B3.

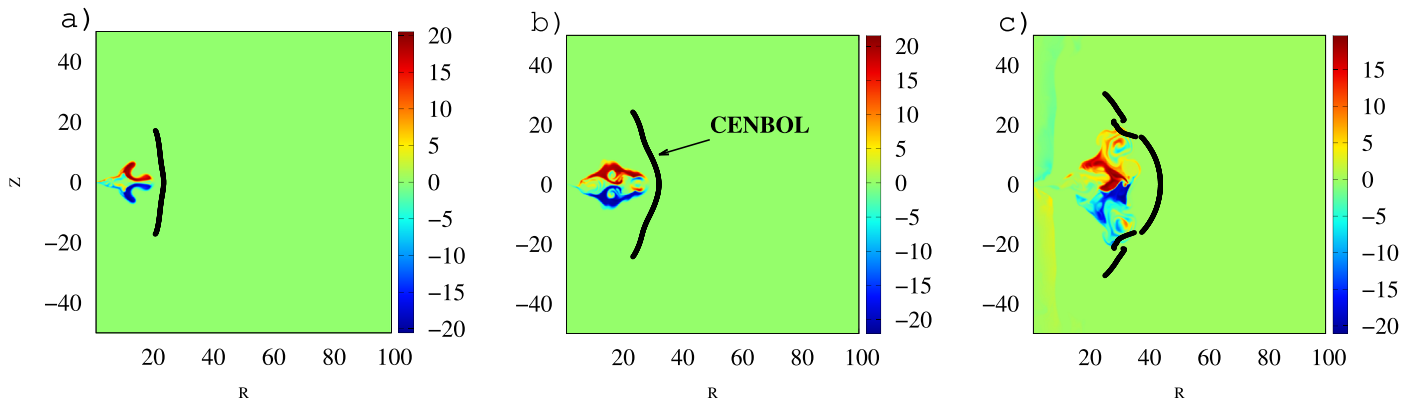


Figure 4. Distribution of the toroidal component of magnetic fields inside the accretion disk for three different cases, A1, A2, and A3, with plasma beta of (a) 50, (b) 25, and (c) 10, respectively. The snapshots are drawn at a time of $18,578r_g/c$, and the specific angular momentum is 1.65 for all three cases. The thick solid black line shows the shock surface (i.e., CENBOL). We see that the toroidal field has opposite signs above and below the equatorial plane. This is caused by the differential toroidal velocity. In the toroidal direction, the stretching of the field varies with radius because of the differential toroidal velocity. However, since the magnetic field directions above and below the equatorial planes are opposite, the toroidal field also attains the opposite sign.

radial direction. The front end moves with the higher radial speed, whereas the rear end moves with the lower radial speed, thus stretching the flux ropes in the radial direction. We further notice that the toroidal component of the flux ropes attains a positive value above the midplane, whereas the same attains a negative value below the midplane. This happens as a result of the differential rotation of matter inside the disk. Matter close to the black hole has a higher toroidal velocity as compared to the matter that is at higher radial distance from the black hole. Thus, the stretching of the field lines in the toroidal direction by the matter, which is attached to the front end of the flux tube, is more compared to the same by the matter, which is attached to the rear end. Since the field lines of the initial flux ropes above the midplane are directed toward the black hole (B_R has negative sign), this differential stretching generates a positive toroidal magnetic field component. Similarly, since the field lines below the midplane are directed away from the black hole, the differential stretching generates a negative toroidal magnetic field component. Figures 4(a)–(c) show the toroidal field component for cases A1, A2, and A3, respectively, at a time of $18,578r_g/c$. By this time, the first episode of flux ropes has reached the CENBOL region. The amplitude the toroidal component is further increased owing to shock compression in this region. We clearly see that the toroidal component above the equatorial plane has positive values, whereas the same below the equatorial plane has negative values. Note also that as the field strength is increased (from panel (a) to panel (c)) the

flux tube becomes more buoyant and expands away from the equatorial plane.

An interesting finding emerging from our simulations is the presence of matter with negative specific angular momentum of the flow as the flux ropes propagate through the sub-Keplerian disk. Since the net angular momentum should be constant in a nondissipative system, the flow may acquire negative angular momentum at the cost of magnetic angular momentum. Figures 5(a)–(c) show the specific angular momentum distribution inside the accretion disk for cases A1, A2, and A3, respectively. The snapshots are taken at a time of $18,578r_g/c$ for all three cases. We see that the angular momenta mostly have a constant value of 1.65 everywhere except in some locations in the post-shock region, wherever the field has penetrated. The thick solid black line shows the shock surface (i.e., CENBOL). Specifically, we can see the generation of negative and large positive angular momentum inside the CENBOL. This is caused by the component of Lorentz force that acts in the toroidal direction in the R – Z plane. When the field loops reach the post-shock region, they are compressed and the magnitude of the magnetic field is increased. The torque associated with the azimuthal component of Lorentz force (L_ϕ) causes the drift of angular momentum from the inner to the outer edge of the field loop. Within the field loop, the azimuthal component of Lorentz force can be written as $L_\phi = v_Z B_R - v_R B_Z$. For our field loops, close to the midplane, the field lines are mostly vertical ($B_R \sim 0$) and therefore

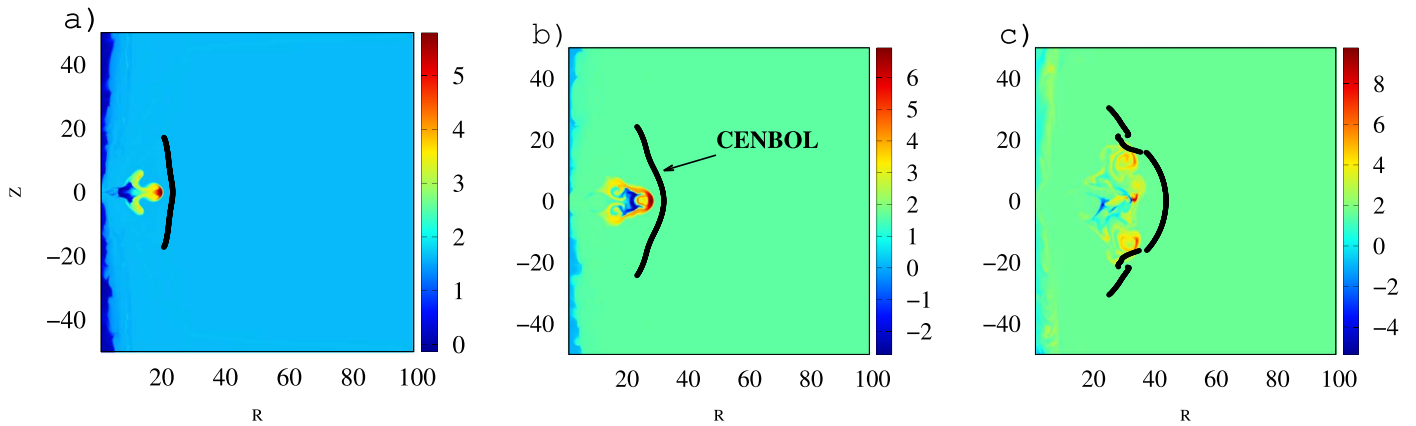


Figure 5. Specific angular momentum distribution inside the accretion disk for cases A1, A2, and A3, with plasma beta of (a) 50, (b) 25, and (c) 10. The snapshots are at $t = 18,578 r_g/c$. We find that the angular momenta mostly have a constant value of 1.65 everywhere except in some locations in the post-shock region. The thick solid black line shows the shock surface (i.e., CENBOL). Specifically, we can see the generation of negative and large positive angular momentum. As the strength of the magnetic field is increased (e.g., plasma beta of 10), the magnitudes of the positive and negative angular momentum are also increased. Notice the change of color scale from panel (a) to panel (c). See text for details.

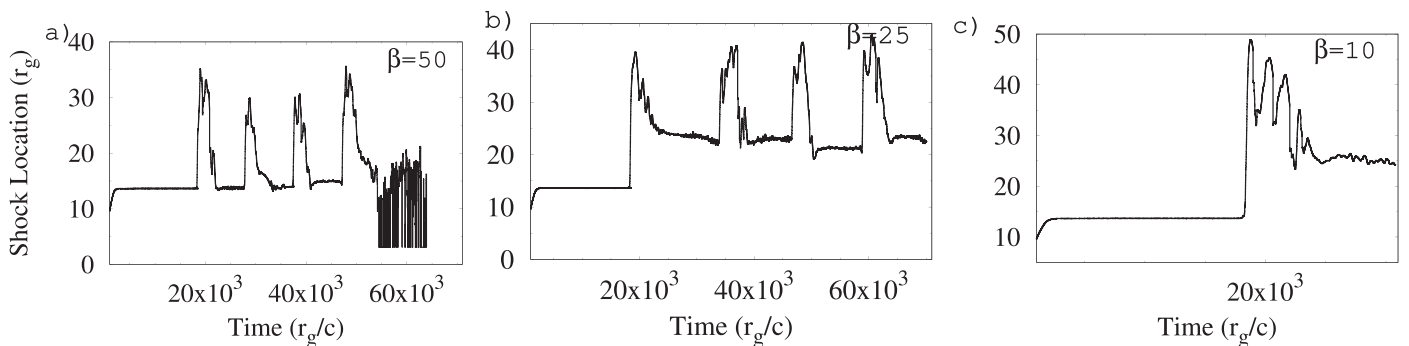


Figure 6. Time variation of the shock location on the equatorial plane of the accretion disk when magnetic flux ropes, with a helical field, are injected into the flow. We show three different cases A1, A2, and A3 with plasma beta of (a) 50, (b) 25, and (c) 10. The specific angular momentum of 1.65 is used for all the cases shown here. Panels (a) and (b) show four episodes of flux rope injection, while panel (c) shows only one such episode. We see that the shock location moves farther out with increasing magnetic field strength (i.e., smaller plasma beta) owing to the joint combination of the thermal and magnetic pressures.

$L_\phi \sim -v_R B_Z$. Since the matter mostly moves toward the black hole, v_R has a negative sign. Also, the front end of the flux ropes has field lines with negative values of B_Z , whereas the rear ends have positive values. Therefore, Lorentz force acts oppositely on the two ends of the field loop and forces the matter on the front end to have negative angular momentum and the matter on the rear end to have large positive angular momentum. As the strength of the magnetic field is increased (e.g., plasma beta of 10, i.e., case A3), the magnitudes of the positive and negative angular momentum are also increased (notice the changing color scale from Figure 5(a) to Figure 5(c)). If we concentrate on the equatorial plane, in all three cases, we find that the angular momentum gradient is positive, i.e., angular momentum is transported outward. This is thus a demonstration that a magnetic viscosity can work inside an accretion disk. However, the appearance of oppositely rotating matter needs to be revisited in more detailed three-dimensional simulations in our future work. Our findings for the propagation of flux ropes are very much similar to what is described in Section 3.1 of Rozyczka et al. (1996). As discussed in this reference, many of these effects are a manifestation of magnetorotational instability as discussed by Hawley & Balbus (1991) and Balbus & Hawley (1991).

3.2. Effects of Magnetic Field on the CENBOL

As the flux ropes arrive at the CENBOL region, the magnetic field is amplified owing to the shock compression. This, in turn, increases the magnetic pressure inside the CENBOL region. Thus, the CENBOL is expanded in both the radial and vertical directions. Some of the infalling matter, along with magnetic field, leaves the computational domain through the top and bottom Z-boundaries as an outflow/jet. This releases the total pressure in the CENBOL region, and the CENBOL tries to go back to its original, unmagnetized configuration. Since the magnetic field is torn apart, it does not leave completely in one go. Rather, it leaves part by part, causing oscillations of the CENBOL. It is interesting to note that we never find a complete destruction of CENBOL for any of the cases presented here. This is mainly because of a sustained supply of spiraling flow that creates a permanent centrifugal barrier. This also demonstrates the stability of the axisymmetric shock in the presence of strong magnetic fields.

Figure 6(a)–(c) show time variation of the shock location on the equatorial plane of the accretion disk for cases A1, A2, and A3, respectively. Initially, we find the steady-state shock to be located at $13 r_g$ in all these cases. When the first flux rope arrives in the CENBOL region, the shock location moves momentarily farther out from the central black hole. However, it slowly moves

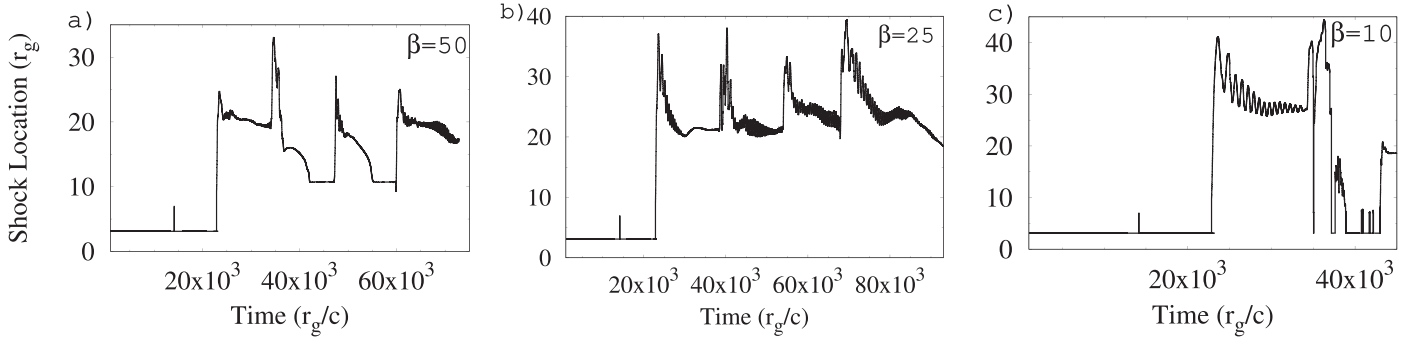


Figure 7. Same as in Figure 6, but with a specific angular momentum of 1.50 (cases B1, B2, and B3). Panels (a) and (b) show four episodes of flux rope injection, while panel (c) shows two such episodes. In this case, the nonmagnetized flow does not have a shock on the equatorial plane. However, a shock is formed when the field rope is present, and it moves farther out with increasing magnetic field strength (i.e., smaller plasma beta).

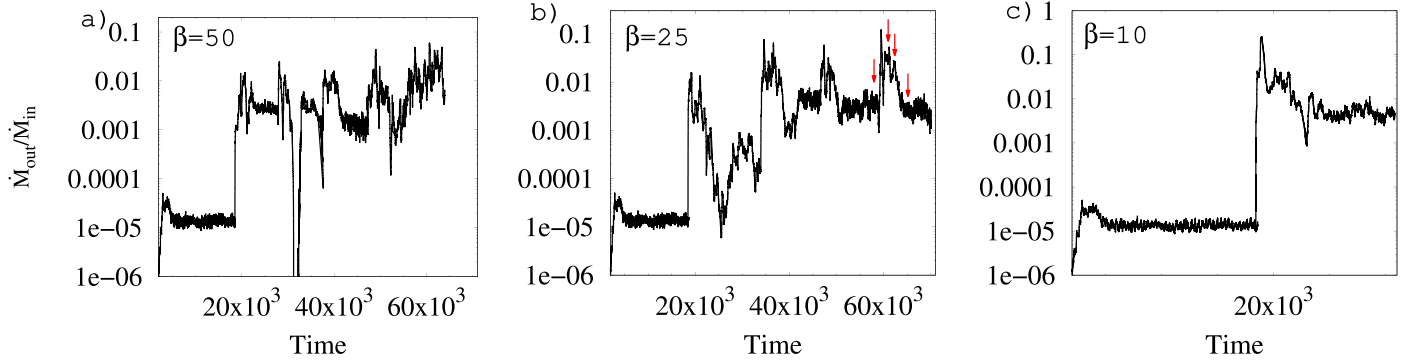


Figure 8. Time variation of the ratio of the total mass outflow through the top and bottom Z-boundaries to the mass inflow through the right radial boundary. Plasma betas are (a) 50, (b) 25, and (c) 10 (cases A1, A2, and A3, respectively). The specific angular momentum of 1.65 is used for all the cases shown here. We see that the mass outflow is significantly enhanced by the presence of magnetic field. Specifically, for a plasma beta of 10 (strong field), nearly 25% of injected matter can leave through the outer boundaries. The nature of the outflow is episodic and almost simultaneous with the time during which the flux tubes stay within the CENBOL.

closer to the black hole and stabilizes at a somewhat intermediate location before the next set of flux ropes arrive at the post-shock region. The intermediate location on the field strength. If the field is weak and is removed from the region, the resulting shock is located at the same place as the hydrodynamic shock. If the field is stronger (panels (b) and (c)), the shock settles to a larger distance owing to leftover field pressure. The shock location after successive injection depends on the strength of the residual field in the post-shock region. Furthermore, the shock does not settle to the resulting location smoothly. Rather, it oscillates a few times, and the frequency increases with decreasing field. For weak fields, the oscillations are not well defined, but they look more prominent as the field becomes stronger, since the magnetic tension prevents quick expansion of the flux tubes. Our work is the first to show that magnetized flow also has quasi-stable shock waves around the black hole.

Figures 7(a)–(c) show the time variation of the shock location on the equatorial plane for cases B1, B2, and B3, respectively. For these cases, the hydrodynamic flow does not have a shock. However, due to the presence of nonzero angular momentum, the flow has a centrifugal barrier, and the matter slows down as it approaches the black hole. Thus, a CENBOL is formed for this case as well. Since the important ingredient of the shock is the centrifugal force, which is very weak in this case, even the weakest field pressure was a significant addition of the pressure in the CENBOL, which causes the formation of shocks. As in the previous cases, the shock momentarily moves far away from the black hole and then stabilizes at a somewhat intermediate location. In all the cases the shock remains owing

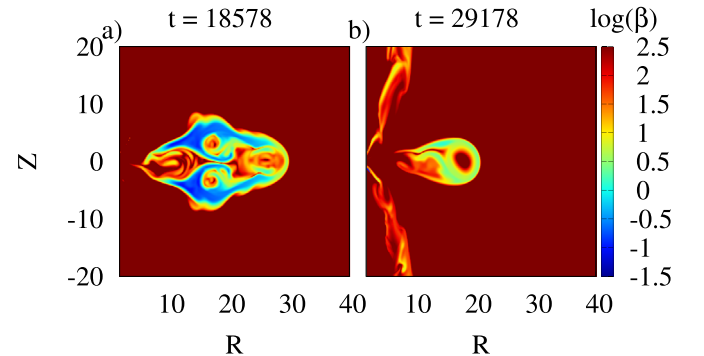


Figure 9. Distribution of plasma beta (β) inside the accretion disk. The figure has been drawn for run A2, and initial β is 25 for this run. (a) β after the field ropes arrived and compressed inside the CENBOL region. Color bar shows that the β value goes down below 0.1, which clearly demonstrates that magnetic pressure increases by at least 2 orders of magnitude compared to the thermal pressure inside some part of CENBOL region. (b) β at a later time when part of the magnetic flux left the CENBOL region and the flow reached a steady state.

to magnetic pressure. Furthermore, the amplitude of oscillation of the shock is low, since the centrifugal force itself is small. For the weakest field the oscillation frequency is higher, but the amplitude is lower. As before, the shock location moves farther out as the strength of the magnetic field increases.

3.3. Effects of Magnetic Field on the Outflow

Figures 8(a)–(c) show time variation of the total outflow for cases A1, A2, and A3, respectively. On the y-axis, we plot the

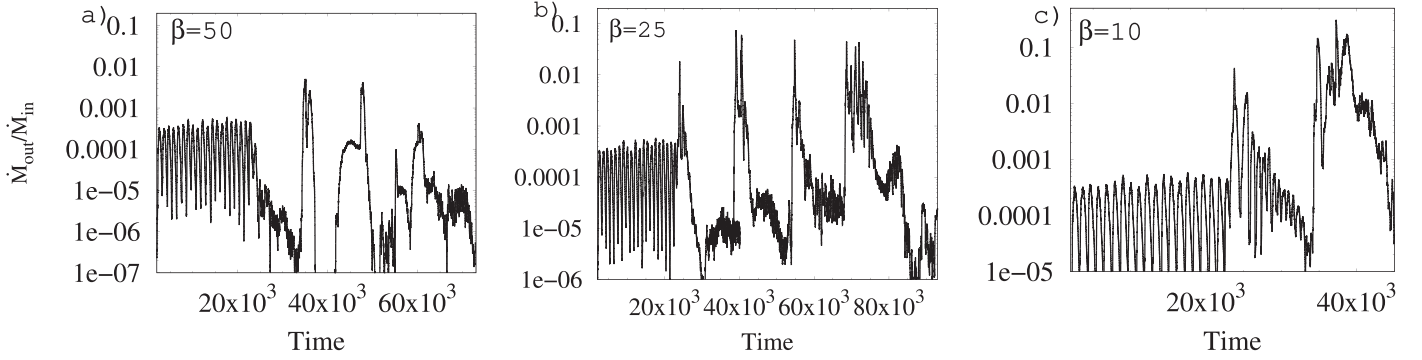


Figure 10. Same as Figure 8, except that the specific angular momentum of 1.50 is used (cases B1, B2, and B3, respectively). Here again, we can see that the mass outflow is significantly enhanced in the presence of the magnetic field. Also, for the plasma beta of 10, nearly 25% of injected matter can leave through the outer boundaries even for this lower angular momentum accretion flow.

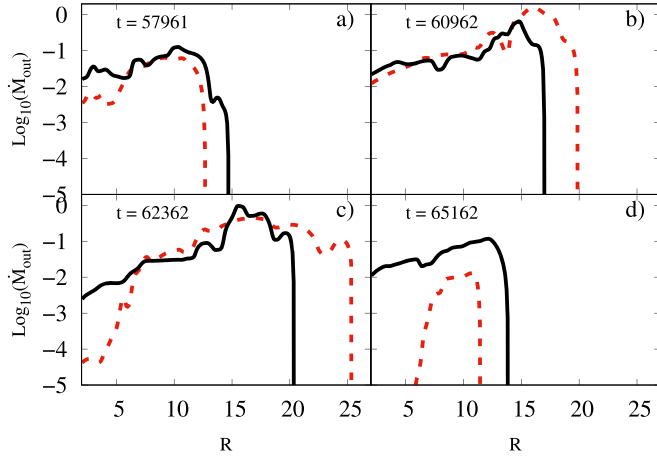


Figure 11. Radial variation of the mass outflow through the upper (dashed red) and lower (solid black) Z-boundaries at four different times marked by four arrows in Figure 8(b). Mass outflow through both the Z-boundaries, placed at $50r_g$ away from the black hole, takes place mostly through the region close to the axis. This shows that the outflowing matter is not wind-like; rather, it forms a collimated jet. Specific angular momentum of 1.65 and a plasma beta of 25 are used (case A2). The jet power flip-flops in the upper and lower quadrants.

ratio of the total outflow rate (\dot{M}_{out}) through the top and bottom Z-boundaries to the total inflow rate (\dot{M}_{in}) through the right radial boundary. Since the specific angular momentum is low ($\lambda = 1.65$), we do not notice significant outflow during the initial unmagnetized accretion flow. This is because the outflow is centrifugally driven. In our simulations, the magnetic field passes through the standing strong magnetosonic shock. As a result, the post-shock field is significantly amplified, increasing its ability to drive outflows. Thus, as soon as the first flux rope arrives at the CENBOL region, the ratio of outflow to inflow is increased by 2–3 orders of magnitude. Specifically, for case A3 ($\beta = 10$, i.e., strong magnetic field), nearly 25% of the injected matter can leave through the outer boundaries. The enhancement of the magnetic pressure in the CENBOL is due to compression, and as a result, it pushes the CENBOL boundary outward, increases the area of the base of the jet, and drives a large fraction of inflow toward the vertical direction (see Figure 9). After the total pressure of the CENBOL region is reduced, the shock returns (Figures 6(a)–(c)) to a smaller radius, and the outflow rate is also reduced before the next flux rope arrives. Thus, the mass flux is also controlled by the flux tube. It is to be noted that each flux rope, after being sheared by differential motion, stays inside the CENBOL for a substantial

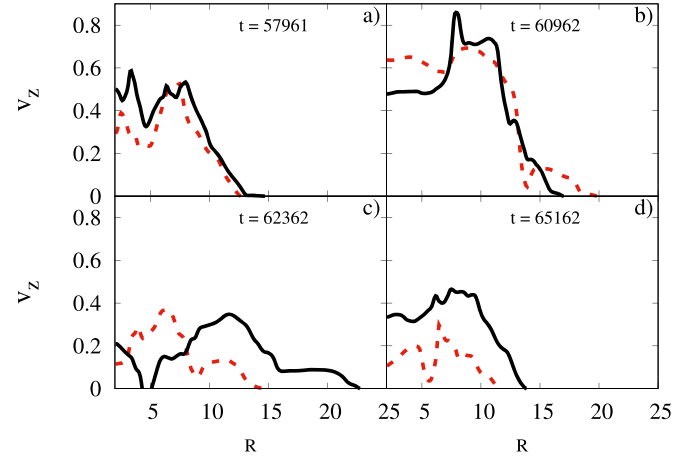


Figure 12. Radial variation of the z-component of velocity of the outflowing matter through the upper (dashed red) and lower (solid black) Z-boundaries at four different times, same as in Figure 11. For lower boundary, the sign of V_z has been flipped for the purpose of comparison. We see that the outflowing matter has the higher ejection velocity close to the axis, showing the collimated nature of the outflow.

amount of time during which it drives the outflow. Figures 10(a)–(c) show the time variation of the outflow rate for cases B1, B2, and B3, respectively. Here, again, we notice a similar behavior to that in the previous cases. The outflow rate is correlated with the shock location shown in Figures 7(a)–(c). We now focus on the collimation properties of the outflowing matter. We consider case A2 for our analysis. Figure 11 shows the radial variation of the mass outflow rate (\dot{M}_{out}) through the upper (dashed red) and lower (solid black) Z-boundaries located at $z = 50$ and $z = -50$, respectively, at four different times marked by four red arrows in Figure 8(b). Figure 11(a) shows the outflow rate just before the initiation of the fourth flux rope injection. By this time, the third flux rope has passed the CENBOL region, and the disk has achieved a stable configuration. The outflow through both the Z-boundaries is found to be taking place close to the axis of rotation. Figures 11(b)–(c) depict the outflow just after the flux rope has entered the CENBOL. The outflow rate is found to be increased by an order of magnitude, which is expected. Even for these two configurations, the outflow is found to be taking place mostly close to the axis of rotation. Finally, Figure 11(d) shows the stabilized state, and again, the rate is higher close to the axis. All these figures show that outflowing matter is not

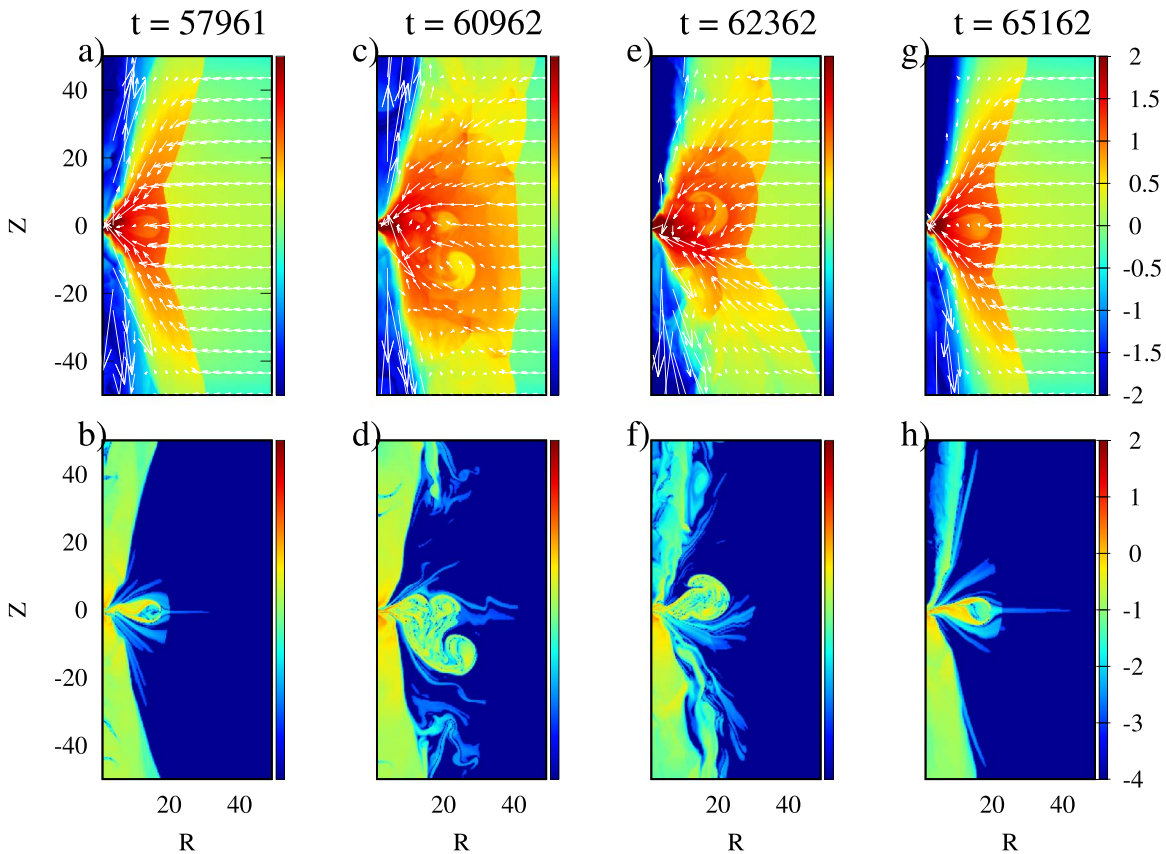


Figure 13. Overall picture of the simulation flow close to the black hole, where we see the inflow, outflow, and the B_ϕ distribution inside the disk. Panels (a), (c), (e), and (g) show the density distribution on log scale, overplotted with velocity vectors, at four different times as in Figure 11 and Figure 12. Panels (b), (d), (f), and (h) show the absolute value of B_ϕ , in log scale, at the same times. We see that the outflowing matter with very high velocities is bound by the toroidal component of the magnetic field. In other words, B_ϕ helps to collimate the outflow. The specific angular momentum of 1.65 and a plasma beta of 25 are used for this case (run A2).

wind-like with high opening angle; rather, the matter leaves the disk in a jet-like collimated fashion.

To further prove the collimation of the outflow, in Figure 12 we plot the radial variation of V_z of the matter flowing through the upper (dashed red) and lower (solid black) Z-boundaries at the same four times as in Figure 11. Outflowing matter through the upper Z-boundary has a positive velocity, whereas the same through the lower Z-boundary has a negative velocity. The sign of V_z has been flipped while plotting for the lower Z-boundary. These plots show that the higher velocity outflowing matter truly leaves the computational domain very close to the axis, showing the collimated nature of the outflow.

In order to explore the reason for the collimation, we investigate the correlation between the outflow and the toroidal component of magnetic field (B_ϕ). Figures 13(a), (c), (e), and (g) show the density distribution on log scale, overplotted with velocity vectors, at four different times as in Figure 8 and Figure 10. Figures 13(b), (d), (f), and (h) show the absolute value of B_ϕ , again on log scale, at the same times. We clearly see that the outflowing matter with very high velocities is bound by the toroidal component of the magnetic field. Thus, B_ϕ helps to collimate the outflow owing to the so-called “hoop-stress” (see also CD94 and DC94).

Figure 14 shows how magnetic flux escapes from the disk. We have shown the zoomed-in snapshots at four different times (marked on the top of each snapshot) in the upper quadrant of the computational domain for run A3. Poloidal magnetic field lines are shown by white lines, and the velocity vectors of the matter are shown by the black arrows. The magnetic flux is

seen to be escaping through the initially empty funnel area. Incoming poloidal field loops first enter the low-density area close to the axis and subsequently expand to form large-scale poloidal field lines. The length of the velocity vectors confirms that the matter in this region also achieves a high velocity parallel to the magnetic field lines.

3.4. On the Question of Anchoring of the Flux Tubes

In stars with radiative core and convective envelope it is well known that the magnetic fields are anchored in between these two strata and may from time to time be buoyant and partly leave the convective envelope creating structured corona. Random motions of the convective zones often reconnect the flux tubes, and the magnetic energy heats up the corona. In the case of accretion disks, it is customary to assume a corona without proving that magnetic field lines could be anchored. Preliminary studies of this by CD94 and DC94 suggest that only if the entropy gradient is favorable, as in the stars, sometimes the flux tubes will be trapped and oscillate. In the present context we have seen the oscillation of the flux tubes inside the CENBOL as well. Thus, instead of leaving the disk as a whole, the torn flux tube leaves part by part, in the form of toroidal loops. As in stars, the possibility of this behavior depends on the entropy gradient. In stars, for stability reasons, entropy must go down toward the surface, as well as toward the center.

In Figures 15(a)–(l), we present the entropy map of the flow at roughly equidistant time during the interval of our interest:

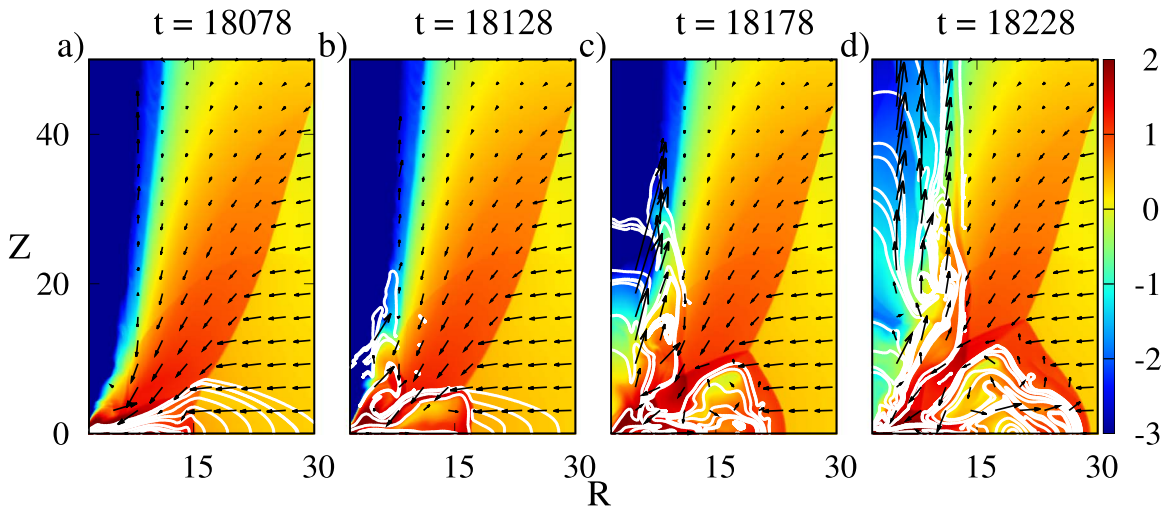


Figure 14. Escape of magnetic flux from the disk. Zoomed-in snapshots at four different times (marked on the top of each snapshot) in the upper quadrant are shown here. The color shows the logarithm of density. White lines show the poloidal magnetic field lines, and black arrows show the velocity vectors. This figure has been drawn for run A3.

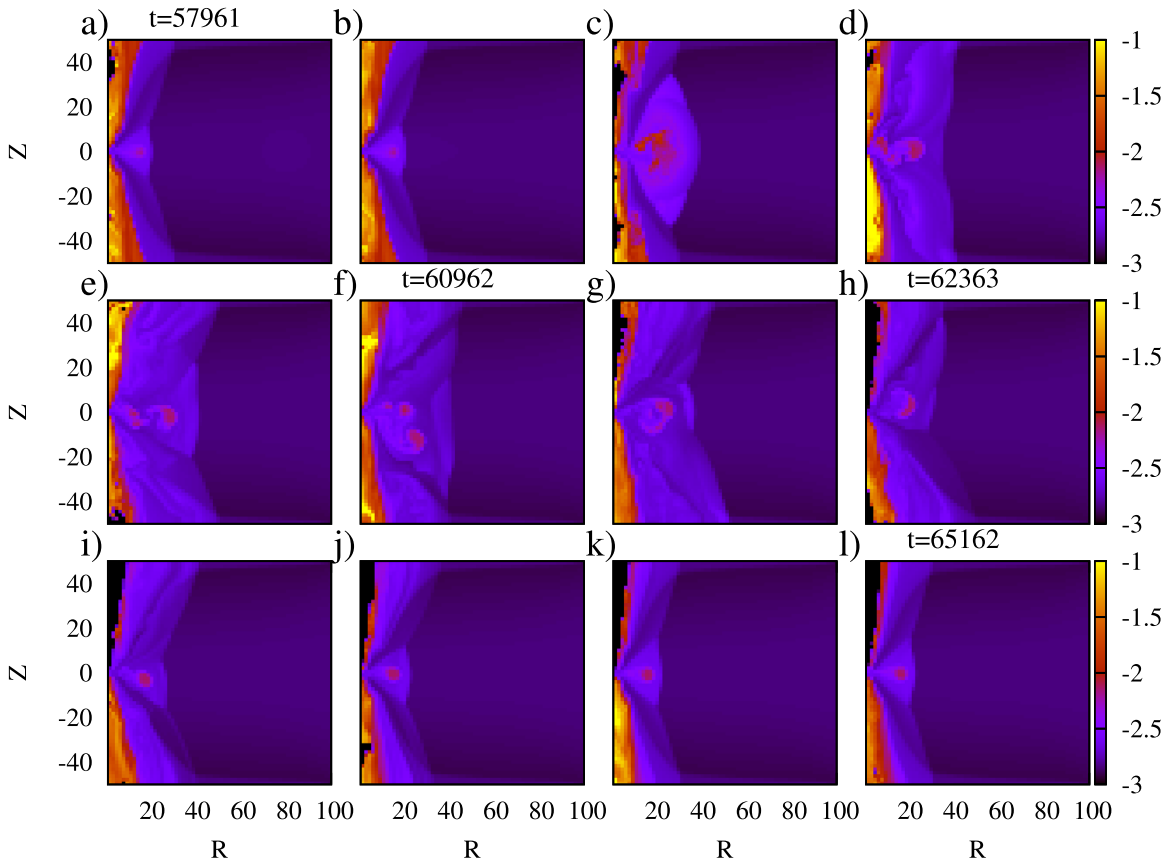


Figure 15. Entropy (P/ρ^γ) distribution in log scale at nearly equidistant times between $t = 57,961$ and $65,162$. The panels marked “ $t = \text{xxxx}$ ” are drawn at the same time as in Figures 11–13. The extra panels are added to get a better understanding of the time evolution of entropy. The zones are rebinned on a 16×16 mesh in order to have coarse grid data. In the black regions, the mass density is less than 1% of the injected density.

$t = 57,961$ to $65,162$. A 16×16 course grid is chosen to avoid very small scale variations. The color scale shows that a high-entropy blob expands in all directions and then collapses. This is the behavior of the shock location as well. Second, highest-entropy flow forms along the axis where the matter escapes after passing through the CENBOL. In Figures 16(a)–(p), we present the vertical and radial entropy gradients at the

same times when Figures 11–13 were drawn in a zoomed-in region close to the black hole. The rows from top to bottom show in colors, respectively, (a–d) entropy gradients in the vertical direction (dS/dZ), (e–h) radial gradient (dS/dR), (i–l) the magnitude of the net field $\sqrt{(B_R^2 + B_\phi^2 + B_Z^2)}$ in log scale, and (m–p) the magnitude of the B_ϕ component in log scale. The corresponding color scales are placed on the side. The arrows

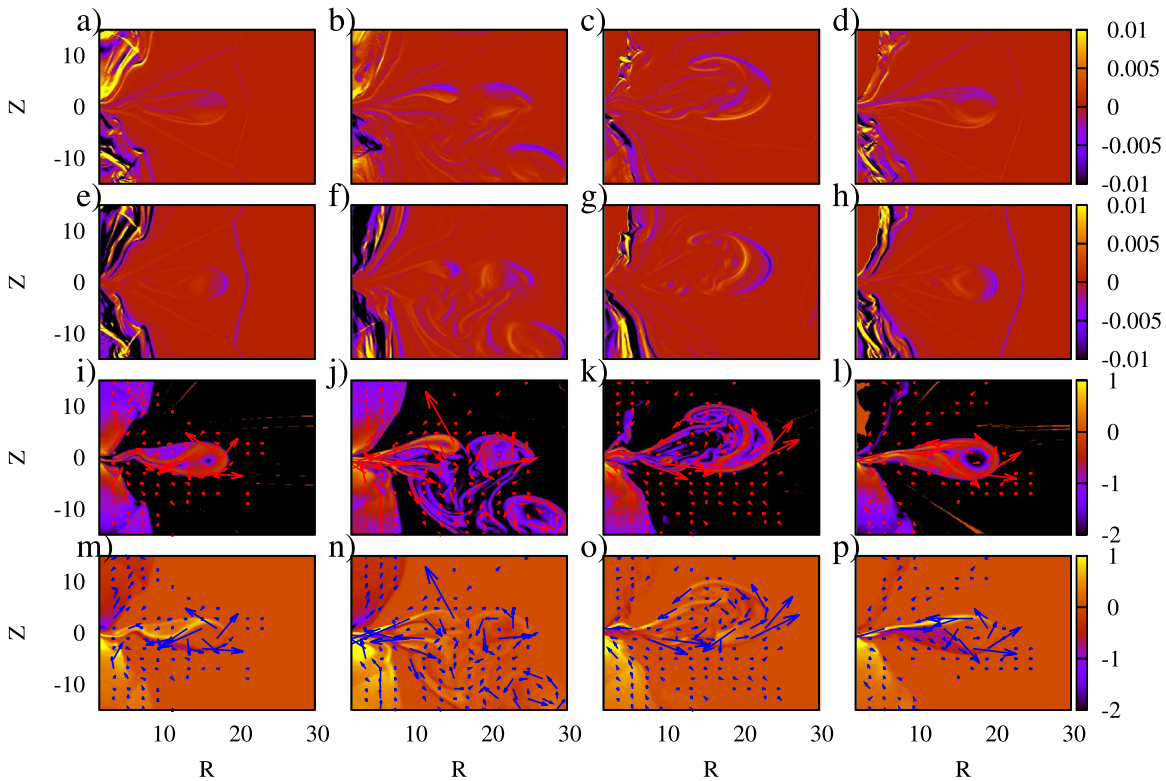


Figure 16. First row (panels (a)–(d)) shows the dS/dZ distribution at four different times ($t = 57,961, 60,962, 62,363,$ and $65,162$). The second row (panels (e)–(h)) shows dS/dR at the same times. The color scales are chosen so that the variation is visible. The third row (panels (i)–(l)) shows $\sqrt{B_R^2 + B_\phi^2 + B_Z^2}$ distribution in log scale at those times. The fourth row (panels (m)–(p)) shows the distribution of B_ϕ in linear scale. Here the lower limit of the color scale has been set to -2 , but the upper limit represents the true maximum value of the data. Vectors represent (B_R, B_Z) field, and their lengths are proportional to $\sqrt{B_R^2 + B_Z^2}$.

represent the field direction in the R – Z plane. The lengths are proportional to $\sqrt{B_R^2 + B_Z^2}$. In the black regions, the mass density is less than 1% of the injected density. We note very interesting behavior: the vertical gradient is very strongly negative in the upper hemisphere and weakly positive in the lower hemisphere. This drives the magnetic blob upward. Similarly, the radial gradient is negative at the forefront of the expanding bubble. This also drives the flux tube away from the axis, except that, owing to resistance of the inflow upstream, the field mostly escapes vertically. From the arrows, we see a strong helicity in the flux rope. We also note that B_ϕ is strong in the lower jet, causing a strong expulsion of fluxes along the axis. So, while inside the disk the flux is driving toward the upper hemisphere, inside the jet the field (from previous episodes) already escapes through the lower jet. We generally find that the funnel region along the axis is magnetically very active, and a high degree of reconnection cannot be ruled out. When such energy dissipation is included in the code in the future, we anticipate that a higher outflow rate would be seen.

4. Conclusions

In this paper, we have studied several aspects of a rotating transonic (advective) flow in the presence of magnetic flux tubes. In the literature, much of the studies have been made only with hydrodynamic flows. These studies showed, both theoretically and with numerical simulations, how standing shocks could form in between two sonic points during its passages toward the black hole. However, in a realistic accretion, significant magnetic activity could be present that might disrupt the flow or convert the flow to a Keplerian disk in

case the magnetic transport of angular momentum were large enough. Also, the magnetic fields may also contribute to accelerate and collimate matter in the outflow. Thus, it is very important to study the effects of magnetic fields on the accretion and outflows. Following CD94 and DC94, Deb et al. (2017) recently showed that a single flux tube may be able to collimate the jet and outflow coming out of the post-shock region. However, they used a hydrodynamic code that treated the fields passively.

In the present paper, we used an ideal MHD code and applied it around a Schwarzschild black hole geometry. As a starting point, we wanted to study the effects of toroidal flux tubes that were injected from the outer boundary. We assumed that the random magnetic fields are sheared predominantly owing to the rotational velocity close to the black hole and that the fields are predominantly toroidal in shape. These flux tubes could have various strengths or cross sections. However, we select only a single cross section. Similarly, we also injected these field lines one by one, while in reality the situation could be more complex and many field lines may be entering simultaneously.

Even with this simple consideration, we established a few very important results. First of all, we show that the flux tube strengthens the formation of the shock wave and repeated bombardments of the flux tube do not destabilize the shock front or the flow geometry at all. This is important, since the post-shock region behaves as the hot Compton cloud that inverse Comptonizes the soft photons and produces a power-law photon in a typical disk spectrum (Chakrabarti 1997; Ghosh et al. 2009, 2010; Garain et al. 2012, 2014). Second, the flux tubes are sheared as they propagate close to the black hole and are ejected

along the vertical axis. The funnel region is found to have high entropy and is also magnetically very active. The outflows are found to be collimated with high-velocity components. We also notice that along the direction in which entropy decreases, the flux tubes escape, very similar to what happens in a star with a radiative core and convective envelope (like our Sun). However, they were not seen to form coronae as on the solar surface since the regions of highest entropy are highly dynamic and anchoring flux tubes become difficult.

In the presence of magnetic flux tubes, the field pressure adds up with the thermal pressure inside the CENBOL region, making the shock location at a higher radius. The shock ejects the flux tubes oscillating back and forth, thereby modulating the outflows as well. Furthermore, we find that the flux tube is ejected asymmetrically in the upper and lower quadrants.

A phenomenon discovered by us may be important: we find that typically the matter loses angular momentum at the inner half inside the flux tube and gains it at the outer half. They are radially stretched by this process and also due to differential radial velocity. Thus, the flux tubes may be used to transport angular momentum inside the disk as well.

In the literature, use has been made of large-scale magnetic field lines for jet formation and collimation. While it is unclear how these field lines are generated, we find that generically obtained flux tubes such as those we use here can perform equally well in acceleration and collimation. Rapid expulsion of flux tubes along the vertical axis may also eject relativistic blobs of matter. Thus, both the compact and blobby jets are possible in our configuration. These aspects and the effects of such magnetized flows on disk spectrum will be studied in the future and will be reported elsewhere.

D.S.B. acknowledges support via NSF grants NSF-ACI-1533850, NSF-DMS-1622457, NSF-ACI-1713765. Several simulations were performed on a cluster at UND that is run by the Center for Research Computing. Computer support on NSF's XSEDE and Blue Waters computing resources is also acknowledged. S.K.C. acknowledges a grant from Higher Education Dept. of the State of West Bengal. J.K. acknowledges the support by Basic Science Research Program through the National Research Foundation of Korea (NRF) funded by the Ministry of Education (2018R1D1A1B07042949) and National Supercomputing Center with supercomputing resources including technical support (KSC-2018-CRE-0098).

Software: RIEMANN code (Balsara 1998a, 1998b, 2004, 2009; Balsara & Spicer 1999b, 1999a; Balsara et al. 2009, 2013).

ORCID iDs

Sudip K. Garain  <https://orcid.org/0000-0001-9220-0744>

Sandip K. Chakrabarti  <https://orcid.org/0000-0002-0193-1136>

References

- Balbus, S. A., & Hawley, J. F. 1991, *ApJ*, 376, 214
 Balsara, D. S. 1998a, *ApJS*, 116, 119
 Balsara, D. S. 1998b, *ApJS*, 116, 133
 Balsara, D. S. 2004, *ApJS*, 151, 149
 Balsara, D. S. 2009, *JCoPh*, 228, 5040
 Balsara, D. S., Meyer, C., Dumbser, M., Du, H., & Xu, Z. 2013, *JCoPh*, 235, 934
 Balsara, D. S., Rumpf, T., Dumbser, M., & Munz, C.-D. 2009, *JCoPh*, 228, 2480
 Balsara, D. S., & Spicer, D. 1999a, *JCoPh*, 148, 133
 Balsara, D. S., & Spicer, D. S. 1999b, *JCoPh*, 149, 270
 Blandford, R. D., & Payne, D. G. 1982, *MNRAS*, 199, 883
 Camenzind, M. 1989, *ASSL*, 156, 129
 Chakrabarti, S. K. 1986, *ApJ*, 303, 582
 Chakrabarti, S. K. 1989, *ApJL*, 337, L89
 Chakrabarti, S. K. 1990, *Theory of Transonic Astrophysical Flows* (Singapore: World Scientific)
 Chakrabarti, S. K. 1997, *ApJ*, 484, 313
 Chakrabarti, S. K., Acharyya, K., & Molteni, D. 2004, *A&A*, 421, 1
 Chakrabarti, S. K., & Bhaskaran, P. 1992, *MNRAS*, 255, 255
 Chakrabarti, S. K., & D'Silva, S. 1994, *ApJ*, 424, 138
 Coroniti, F. V. 1981, *ApJ*, 244, 587
 Deb, A., Giri, K., & Chakrabarti, S. K. 2017, *MNRAS*, 472, 1259
 D'Silva, S., & Chakrabarti, S. K. 1994, *ApJ*, 424, 149
 Eardley, D. M., & Lightman, A. P. 1975, *ApJ*, 200, 187
 Eggum, G. E., Coroniti, F. V., & Katz, J. I. 1985, *ApJL*, 298, L41
 Fukue, J. 1982, *PASJ*, 34, 163
 Galeev, A. A., Rosner, R., & Vaiana, G. S. 1979, *ApJ*, 229, 318
 Garain, S. K., Ghosh, H., & Chakrabarti, S. K. 2012, *ApJ*, 758, 114
 Garain, S. K., Ghosh, H., & Chakrabarti, S. K. 2014, *MNRAS*, 437, 1329
 Ghosh, H., Chakrabarti, S. K., & Laurent, P. 2009, *IJMPD*, 18, 1693
 Ghosh, H., Garain, S. K., Chakrabarti, S. K., & Laurent, P. 2010, *IJMPD*, 19, 607
 Giri, K., & Chakrabarti, S. K. 2013, *MNRAS*, 430, 2836
 Giri, K., Chakrabarti, S. K., Samanta, M. M., & Ryu, D. 2010, *MNRAS*, 403, 516
 Hawley, J. F. 2000, *ApJ*, 528, 462
 Hawley, J. F., & Balbus, S. A. 1991, *ApJ*, 376, 223
 Hawley, J. F., & Krolik, J. H. 2001, *ApJ*, 548, 348
 Heyvaerts, J., & Norman, C. 1989, *ApJ*, 347, 1055
 Koide, S., Shibata, K., & Kudoh, T. 1999, *ApJ*, 522, 727
 Konigl, A. 1989, *ApJ*, 342, 208
 Kudoh, T., Matsumoto, R., & Shibata, K. 2002, *PASJ*, 54, 267
 Lee, S.-J., Chattopadhyay, I., Kumar, R., Hyung, S., & Ryu, D. 2016, *ApJ*, 831, 33
 Lovelace, R. V. E. 1976, *Natur*, 262, 649
 Lynden-Bell, D. 1978, *PhyS*, 17, 185
 McKinney, J. C. 2006, *MNRAS*, 368, 1561
 Molteni, D., Lanzafame, G., & Chakrabarti, S. K. 1994, *ApJ*, 425, 161
 Molteni, D., Ryu, D., & Chakrabarti, S. K. 1996a, *ApJ*, 470, 460
 Molteni, D., Sponholz, H., & Chakrabarti, S. K. 1996b, *ApJ*, 457, 805
 Nishikawa, K. I., Richardson, G., Koide, S., et al. 2005, *ApJ*, 625, 60
 Paczyński, B., & Wiita, P. J. 1980, *A&A*, 500, 203
 Rozyczka, M., Bodenheimer, P., & Lin, D. N. C. 1996, *ApJ*, 459, 371
 Ryu, D., Brown, G. L., Ostriker, J. P., & Loeb, A. 1995a, *ApJ*, 452, 364
 Ryu, D., Chakrabarti, S. K., & Molteni, D. 1997, *ApJ*, 474, 378
 Ryu, D., Yun, H. S., & Cheo, S.-U. 1995b, *JKAS*, 28, 223
 Shafee, R., McKinney, J. C., Narayan, R., et al. 2008, *ApJL*, 687, L25
 Shibata, K., Tajima, T., & Matsumoto, R. 1990, *ApJ*, 350, 295
 Tchekhovskoy, A., Narayan, R., & McKinney, J. C. 2011, *MNRAS*, 418, L79